The Effect of Dilution on Microsegregation in AWS ER NiCrMo-14 Alloy Welding Claddings

ÉMERSON MENDONÇA MINÁ, YURI CRUZ DA SILVA, JEAN DILLE, and CLEITON CARVALHO SILVA

Dilution and microsegregation are phenomena inherent to claddings, which, in turn, directly affect their main properties. This study evaluated microsegregation in the fusion zone with different dilution levels. The overlays were welded by the TIG cold wire feed process. Dilution was calculated from the geometric characteristics of the claddings and from the conservation of mass equation using chemical composition measurements. Microsegregation was calculated using energy dispersive X-ray spectroscopy measurements of the dendrites and the chemical composition of the fusion zone. The dilution of the claddings was increased by reducing the wire feed rate. Fe showed potential to be incorporated into the solid phase ($k > 1$), and this increased with the increase of dilution. Mo, in turn, was segregated into the liquid phase ($k < 1$) and also increased with the increase of dilution. However, Cr and W showed a slight decrease in their partition coefficients (k) with the increase of dilution.

I. INTRODUCTION

NICKEL-BASED superalloys are special materials that have excellent mechanical properties at high temperatures and show good resistance to corrosion and oxidation.[1] Due to these properties, these superalloys are used in nuclear power plants, the aeronautical industry, components for power-generation turbines, missiles for the arms industry, chemical and petrochemical processing plants as well as in the oil and gas industry.[2] Their excellent resistance to corrosion is associated with a very thin stable oxide layer, which protects the material from the external environment.[3,4] The chromium is responsible for forming the oxide layer, while the molybdenum increases resistance to localized corrosion by promoting repassivation of the oxide film.[5]

The high cost of superalloys limits their application from an economic point of view.[6,7] However, to help overcome this issue, weld cladding is considered an alternative for manufacturing parts and equipment whose external or internal surfaces require specific properties that allow a satisfactory performance under the service conditions required.[6] Nonetheless, several metallurgical aspects of the weld claddings must be considered. For example, the crystalline structures of the substrate and deposit, as well as their properties, tend to make welding much more complex.[8,9] Moreover, there are also various microchemical alterations, such as an increase of Fe and C, as a consequence of the dilution of the deposit with the substrate,[10] as well as microsegregation, which is a phenomenon that results from solidification under unbalanced conditions. Microsegregation also causes significant microchemical and microstructural changes, such as the nucleation of secondary phases.[11] Consequently, microsegregation affects the properties of these alloys and these microchemical alterations tend to potentialize susceptibility to localized corrosion.[12] Thus, a microsegregation evaluation is fundamentally important for applications where resistance to corrosion is required.

The Inconel 686 alloy, the main alloy to be evaluated in this study, is considered to be one of the first third generation nickel-based superalloys. It was developed in 1992 to meet the needs of applications to be used under severe corrosion conditions.[13] The 686 alloy belongs to the Ni-Cr-Mo class with the addition of W, developed, at first, for equipment to purify gas from burning coal, commonly used in thermoelectric plants.[13] In addition to this, its excellent resistance to corrosion in acidic aqueous media has made this alloy interesting for other industries, such as the oil and gas industry.[14,15]

However, few studies have been made with the Inconel 686 alloy, especially studies that evaluate its welded microstructure. This study investigated the effect of dilution in deposits of Inconel 686 alloy on carbon steel, as well as the possible changes in microsegregation.

ÉMERSON MENDONÇA MINÁ and YURI CRUZ DA SILVA, Doctoral Students, and CLEITON CARVALHO SILVA, Professor, are with the Universidade Federal do Ceará, Department of Metallurgical and Materials Engineering, Campus do Pici, Building 1080, Fortaleza, Ceará, 60.455-760, Brazil. Contact e-mail: emina@metalmat.ufc.br JEAN DILLE, Professor, is with the Université Libre de Bruxelles, Brussels, Belgium, and Federal University of Rio de Janeiro, Rio de Janeiro, Brazil.

II. EXPERIMENTAL PROCEDURES

A. Materials

For the weld claddings, the AWS ER-NiCrMo-14 wire was used as the filler metal. The 1.2-mm diameter

wire presents the same specifications as the Inconel 686 alloy. The substrate used was the ASTM A36 structural steel. Table I shows the chemical composition of the materials used. The TIG process, with cold wire feeding, was used to produce the claddings. The welding process used a 4-mm diameter thoriated tungsten electrode, and pure argon was the shielding gas.

B. Methods

An industrial robotic workbench was used to guarantee the welding speed and torch movement. A multi process power supply associated with an automatic cold wire TIG headstock was used to perform the welds. The automatic system to feed the wire into the weld pool allowed a precise control of the wire feeding speed, and thus claddings with different dilution levels could be produced without any alterations of heat input. A robotic TIG torch with a wire positioning system that aligned and adjusted the wire with respect to the electric arc was also employed in the manufacturing of all the claddings. A data acquisition system to measure the welding current and voltage in real time was used to guarantee that the same heat input was applied to produce all claddings.

The claddings were produced with a voltage of 21 V, a current of 380 A, and a welding speed of 21 cm/min. Preheating was not used to manufacture the claddings. For the multipass welding, a 2/3 shift from the initial position of the first pass was used to set the beginning position of the following pass, and an interpass temperature of 373 K (100 °C) was used. Most of the parameters used were based on works previously published in the literature.[14]

The wire feeding speed (S_{wf}) was reduced to obtain increasing levels of dilution, since with less filler metal, more energy will remain to melt the substrate.[16–18] Furthermore, the smaller the amount of filler metal added, the smaller the metal barrier between the substrate and the electric arc will be. Thus, the heat input will act more intensely on the metal base.[18]

Two weaving types were used: spiral and triangular. The spiral weave was chosen, because previous works indicated that if the right parameters were used, this weave type could produce claddings with low dilution, less than 10 pct.[14,18,19] However, the spiral weave is unstable and can cause internal and superficial defects especially when there is a reduction of the wire feeding speed.[14,18,19] Other claddings were manufactured with the triangular wave, which does not present any defects when the wire feeding speed is reduced.[14,18,20] Figure 1 illustrates the types of weave used. The weave amplitude (WA) of 8 mm was used for all claddings done with

triangular weaving. However, for the spiral weave, an amplitude of 6 mm was applied in order to produce a cladding without any defects on the sides of the passes. Table II shows the wire feeding speed and weave, in which S and T represent the Spiral and Triangular waves, respectively, and the numbers represent the values of the wire feeding speed in m/min; for example, S85 corresponds to a spiral weave with a wire feeding speed of 8.5 m/min.

The claddings were cut and subjected to a conventional metallographic preparation, specifically to be able to acquire a cross-section macrograph, as well as for the analyses of scanning electron microscopy (SEM). Chemical etching was performed with 2 pct Nital to revel the base metal and observe the macrographs. To analyze the microstructure of the weld metal by SEM, electrolytic etching was performed with a 10 pct solution of chromic acid.

Two methodologies were employed to calculate the dilution of the claddings. In the first method, the geometrical characteristics of the claddings were used, namely the areas of the base metal (A_{BM}) and filler metal (A_{FM}), which composed the melted zone. Equation [1] shows the formula used to calculate the dilution. The measures of two cross-sections from each cladding were
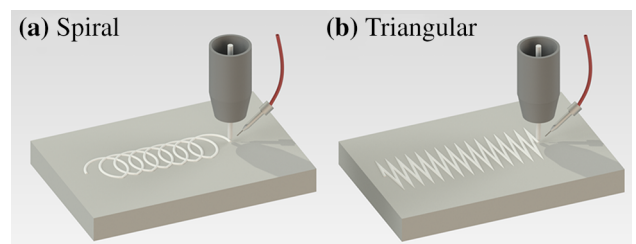

Fig. 1—Illustration of the weave trajectories: spiral (a) and triangular (b).

Table II. Cladding Welding Conditions and their Respective Welding Parameters

Claddings	S_{wf} (m/min)	Weave	WA (mm)
S85	8.5	Spiral	6
T85	8.5	Triangular	8
T75	7.5	Triangular	8
T65	6.5	Triangular	8
T55	5.5	Triangular	8
T45	4.5	Triangular	8

S_{wf}, represents wire feeding speed; WA, represents the weave amplitude.

Table I. Chemical Composition of the Filler Metal and Base Metal (Wt Percent)

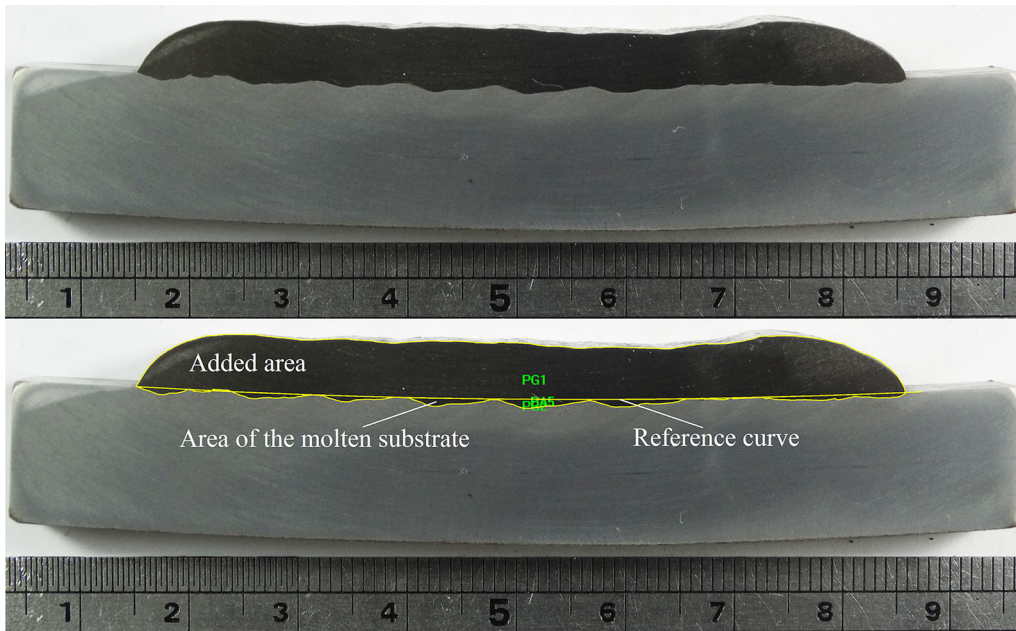| Alloy	Chemical Composition (Pct in Wt)								
	Cr	Mo	W	Si	Fe	C	Mn	Ni	Al
AWS ER-NiCrMo-14 (Inconel 686)	20.53	16.39	3.97	0.06	0.29	0.01	0.23	58.52	—
ASTM A36	0.02	—	—	0.09	98.94	0.23	0.67	0.02	0.03

Fig. 2—Macrograph of the S85 cross-section and its respective geometric analysis.
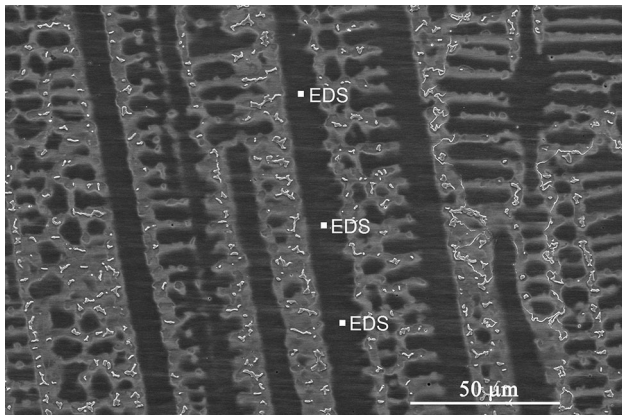

Fig. 3—Micrograph showing the arrangement of the EDS points (wt pct) chemical composition performed in the center of a dendrite, located in the melted zone of T65.
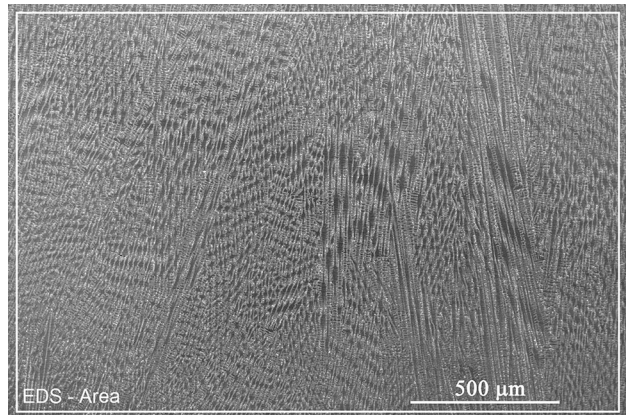

Fig. 4—Micrograph of a given area selected for EDS (wt pct) chemical composition scanning, from the melted zone of T85.

used, and, finally, an average of the claddings dilution was calculated. Figure 2 shows one of the macrographs used to calculate the geometric dilution.

$$D = \frac{A_{BM}}{A_{BM} + A_{FM}} \qquad [1]$$

The second method uses the conservation of mass equation to calculate the dilution. The concentrations of Fe in the fusion zone (C_{FZ}), in the base metal (C_{BM}), and in the filler metal (C_{FM}) were used. Equation [2] gives the dilution level by this method.

$$D = \frac{C_{FZ} - C_{FM}}{C_{BM} - C_{FM}} \qquad [2]$$

The partition coefficient (k) is calculated as shown in Eq. [3]. The dendrites are the first solids to be formed, and, thus, are considered to be the composition of the solid (C_S) at the beginning of solidification. The chemical composition of the liquid (C_0) is considered to be the nominal composition of the weld metal.[6,9,13] Therefore, to carry out this calculation, 30 energy dispersive X-ray spectroscopy (EDS) measurements were performed in several dendrite cores. Also 5 EDS measurements were made in large areas of the fusion zone, in order to obtain the global chemical composition of the fusion zone of each cladding. Each EDS was performed using 15 keV in order to reduce the pear of interaction of the beam around the spot, keeping the proportion to at least 1.5 times higher than the energy of characteristic X-ray peaks of the elements under
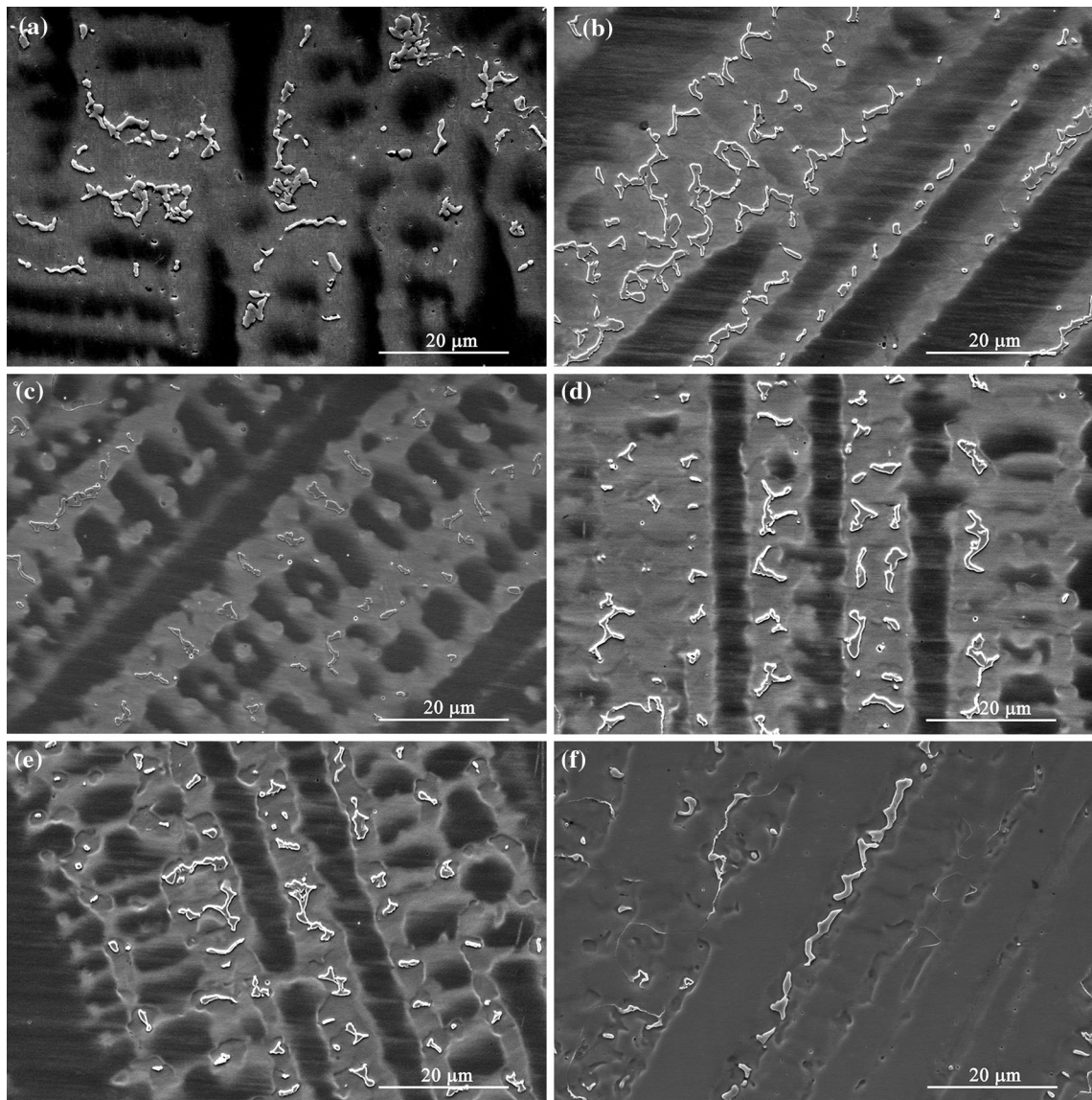
Fig. 5—Microstructure of the melted zone of the claddings. S85 (*a*), T85 (*b*), T75 (*c*), T65 (*d*), T55 (*e*), and T45 (*f*).

analysis. The dead time of the measurements was kept between 20 and 30 pct. All the parameters used followed the recommendations of the ASTM E1245 standard. Also all the results were analyzed according to the ASTM E1245 standard at the 95 pct confidence level for all results. Figures 3 and 4 show the micrographs of the EDS measurements to obtain the chemical composition of the dendrites and the global chemical composition, respectively.

$$k = \frac{C_S}{C_0} \qquad [3]$$

A half of the secondary dendrite arm spacing of each cladding was measured for the Equation proposed by Brody and Flemings[21] with the goal to check if the diffusion during solidification was relevant to be included in the calculation of microsegregation. For each cladding, 10 dendrites were selected from different regions and then various secondary dendrite arms were selected to make an average for each cladding.

III. RESULTS AND DISCUSSION

A. *Dilution*

Table III shows the average and the standard deviation results of the geometric dilution and the dilution based on EDS measurements. The dilution increased as the wire feeding speed was reduced. This phenomenon has already been reported in other studies[16,17] and is related to the lower volume of metal to be melted by the same weld energy. Moreover, this lower volume of wire reduces the barrier between the substrate and the electric arc, thus, allowing the fusion of a greater fraction of the base metal.[16] Both methods had similar results.

Dilution was lower for the cladding deposited by the spiral weave. A similar result was observed by Silva,[14]

who pointed out that the spiral weave promotes an intense movement of the weld pool, moving periodically to colder regions of the plate, thus dissipating more heat when compared to the triangular weave. This result was obtained despite using the same heat input for both weaves (spiral and triangular) that only differ in the movement of the arc.

B. *Microsegregation*

The analysis performed by SEM shows that the melted zone has a microstructure composed of a γ-CFC matrix with some secondary phases. The as-solidified structure of the melted zone displays a columnar dendritic morphology, indicating its solidification mode. This behavior was not found at the interface, which experienced an evolution of the solidification mode, changing from planar to cellular, and from cellular to columnar dendritic along a few hundred microns. On evaluating the columnar dendritic region, which corresponds to most of the as-solidified region, an intense

contrast between the dendrite core and interdendritic region was found. This behavior is probably a consequence of the intense segregation of alloying elements along micrometric distances. Another important observation was the presence of secondary phases formed in interdendritic regions, which were rich in segregated elements, indicating the occurrence of a microsegregation process during the solidification.[14] Despite the

Comparison between the secondary arm spacing of spiral and triangular weave conditions
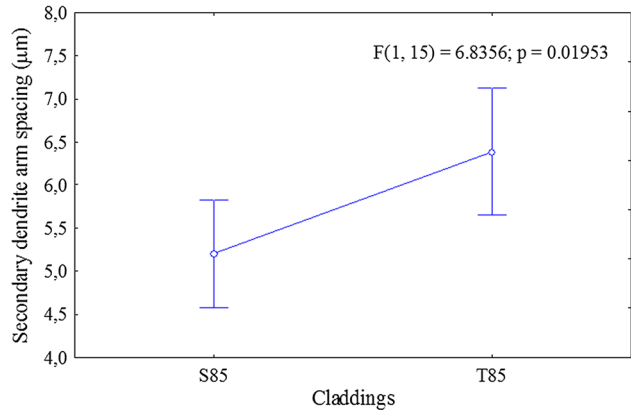
Fig. 7—Secondary dendrite arm spacing comparison between the spiral and triangular weaves.

Table III. Dilution Calculated by Geometric Features and by Chemical Concentration of the Claddings

Claddings	Geometric Dilution	EDS Dilution
S85	7.2 pct ± 0.5	6.0 pct ± 0.5
T85	13.5 pct ± 0.8	12.7 pct ± 0.2
T75	13.6 pct ± 0.7	16.1 pct ± 0.3
T65	18.2 pct ± 1.4	18.0 pct ± 0.5
T55	26.8 pct ± 2.6	24.9 pct ± 0.5
T45	32.6 pct ± 0.7	34.4 pct ± 0.4
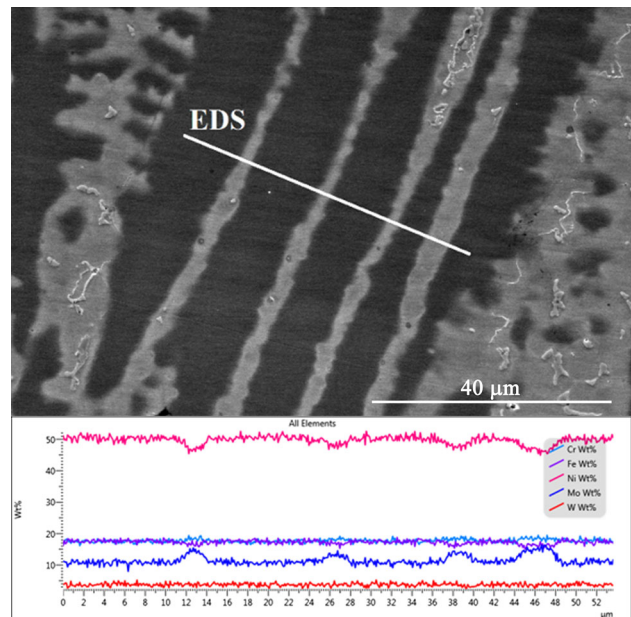
Fig. 8—EDS (wt pct) chemical composition scanning through the dendritic and interdendritic regions located in the melted zone of T75.

Comparison between the secondary arm spacing of triangular weave conditions

Fig. 6—Secondary dendrite arm spacing comparison among the triangular weaves.

Table IV. The Average and the Standard Deviation of the Secondary Dendrite Arm Spacing for All Claddings

Secondary Dendrite Arm Spacing (μm)					
S85	T85	T75	T65	T55	T45
5.2 ± 0.8	6.3 ± 1.0	5.9 ± 0.4	6.5 ± 0.5	5.9 ± 0.4	6.6 ± 1.1

Table V. Beginning of the Solidification Temperature of the Molten Zone of the Claddings

Solidification Temperature (T)					
S85	T85	T75	T65	T55	T45
1643 K (1370 °C)	1652 K (1379 °C)	1649 K (1376 °C)	1647 K (1374 °C)	1649 K (1376 °C)	1654 K (1381 °C)

Table VI. Cooling Rate and the Variation of the Solidification Time for T = 1643 K (1370 °C) and Ts = 394 K (121 °C)

Cladding S85		
T	$\partial T/\partial t$	t_s
1643 K (1370 °C)	383 K/s	1.1 s

Table VII. Diffusion coefficient of the main elements of the alloy and its respective parameters α for t_s = 1, 1 s

Elements	D_s (m²/s)	α
Cr	2.10×10^{-13}[28]	0.037
Fe	1.41×10^{-13}[29]	0.025
Ni	6.25×10^{-14}[30]	0.011
Mo	9.50×10^{-14}[28]	0.017
W	1.61×10^{-14}[28]	0.003
Mn	3.14×10^{-13}[27]	0.055

differences in the compositions between the claddings promoted by the dilution level, the microstructure of the melted zone of each cladding was similar to the one described at the begin of this section. Figure 5 shows micrographs of the center of the melted zone of claddings.

The secondary dendrite arm spacing of each cladding was measured by SEM, and the results showed small differences, even despite using the same heat input to manufacture the claddings. Table IV presents the average and the standard deviation of the secondary dendrite arm spacing of all claddings. The spiral weaves showed the smallest average in comparison to the triangular weaves that presented average values between 5.9 and 6.6 pct. Analysis of variance was performed to check the differences among the triangular weaves as shown in Figure 6. The statistical analyses revealed that the reduction of the wire feeding speed for the same weave parameter (triangular) did not promote relevant differences on the secondary dendrite arm spacing. The comparison between the spiral and triangular weaves, for the same wire feeding speed is shown in Figure 7. Here, a significant difference between the two types of weaves was shown from a statistical point of view. This phenomenon probably is due to the intense motion of the source promoted by the spiral weave which increases the cooling rate and consequently, a reduction of the secondary dendrite arm spacing.

SEM analyses using EDS were performed to check possible changes in the microsegregation. Figure 8 shows an EDS chemical composition profile obtained from T75. The EDS scanning was performed over several dendrite cores and their respective interdendritic regions. The analysis showed that there are changes in the concentrations of the main elements present in the melted zone. Some elements, such as Ni and Mo, had greater changes. In the case of Ni, there was an impoverishment in the interdendritic regions, while, for Mo, there was a higher percentage fraction in the same region. Fe, in turn, showed a slight decrease in its concentration in the interdendritic regions. Cr and W showed no significant changes in this analysis.

The phenomenon of microsegregation, observed in Figures 5 and 8, is usually associated with losses in weldability, changes in solidification temperature and formation of secondary phases.[8] In addition, these deleterious phases create regions susceptible to corrosion on the interface between the matrix and precipitate.[14,15,22] The tendency for microsegregation during solidification can be calculated for each element using measures of chemical composition and classical theories of solidification.

The tendency of a component to segregate or not to the liquid is defined by the partition coefficient k. For a coefficient $k < 1$, the element will segregate to the liquid, while for values of $k > 1$, the element will preferably compose the solid. Normally, it is assumed that the effects of dendrite tip curvature and the diffusion, during the solidification, do not affect the microsegregation. Thus, the microsegregation coefficient can be easily calculated by Eq. [4], known as Scheil's equation,[23] in which C_S represents the composition of the solid, C_0 is the nominal composition of the alloy, and f_S is the fraction of the solid.

$$C_S = kC_0(1 - f_S)^{k-1}. \qquad [4]$$

Brody and Flemings[21] were the first to consider diffusion into the solid during the dendritic solidification when calculating the phenomenon of microsegregation. Equation [5] was proposed by the authors, who took into account that the development of the solid occurred following a parabolic growth at a constant rate and that the phenomenon of diffusion in the solid could only be discarded in systems whose parameter α approached zero.

$$C_S = kC_0[1 - (1 - 2\alpha k)f_S]^{\frac{(k-1)}{(1-2\alpha k)}}. \qquad [5]$$

Parameter α is also known as the Fourier diffusion number. This parameter measures the degree of diffusion of a given solute in the solid. Equation [6] describes the parameter α as the ratio of diffusion coefficient (D_s),

Table VIII. EDS (Wt Pct) Chemical Composition of the Center of the Dendrites of the Claddings

Elements	Chemical Composition of the Center of the Dendrites (Wt Pct)					
	S85	T85	T75	T65	T55	T45
Cr	19.4 ± 0.1	18.2 ± 0.1	17.6 ± 0.2	17.1 ± 0.2	15.4 ± 0.4	13.4 ± 0.1
Fe	6.1 ± 0.5	13.2 ± 0.3	16.7 ± 1.0	18.6 ± 0.7	26.0 ± 1.6	35.6 ± 0.6
Ni	56.6 ± 0.3	52.1 ± 0.2	50.5 ± 0.6	49.0 ± 0.3	44.6 ± 1.0	38.7 ± 0.3
Mo	13.3 ± 0.1	12.3 ± 0.1	11.9 ± 0.1	11.3 ± 0.2	10.4 ± 0.2	9.0 ± 0.1
W	4.4 ± 0.1	4.0 ± 0.1	3.9 ± 0.1	3.7 ± 0.0	3.4 ± 0.1	2.9 ± 0.0
Mn	0.1 ± 0.0	0.2 ± 0.0	0.2 ± 0.0	0.2 ± 0.0	0.2 ± 0.0	0.3 ± 0.0

Table IX. EDS (Wt Pct) Chemical Composition of the Melted Zone of the Claddings

Elements	Chemical Composition of the Melted Zone (Wt Pct)					
	S85	T85	T75	T65	T55	T45
Cr	19.8 ± 0.0	18.4 ± 0.0	17.7 ± 0.1	17.5 ± 0.1	16.0 ± 0.2	14.0 ± 0.1
Fe	5.9 ± 0.5	12.6 ± 0.2	15.8 ± 0.3	17.8 ± 0.5	24.6 ± 0.5	34.0 ± 0.4
Ni	53.5 ± 0.4	49.4 ± 0.1	47.6 ± 0.1	46.9 ± 0.4	42.6 ± 0.3	37.4 ± 0.2
Mo	16.3 ± 0.1	15.4 ± 0.1	14.7 ± 0.1	14.3 ± 0.1	13.1 ± 0.1	11.3 ± 0.1
W	4.3 ± 0.1	4.0 ± 0.0	3.8 ± 0.1	3.7 ± 0.0	3.5 ± 0.1	3.0 ± 0.0
Mn	0.1 ± 0.0	0.2 ± 0.0	0.2 ± 0.0	0.2 ± 0.0	0.3 ± 0.0	0.3 ± 0.0

time variation during solidification (t_f), and half of the dendritic spacing (L).

$$\alpha = \frac{D_S t_S}{L^2}. \qquad [6]$$

To calculate t_s, it is necessary to estimate the cooling rate of the weld during the process, which can be calculated from Eq. [7], which describes the Rosenthal's solution for three dimensions. The calculation of the cooling rate is based on thermal conductivity (λ), weld speed (S_w), beginning of the solidification temperature (T) and pre-heating and/or interpass temperature (T_0), electric arc efficiency (n_a), and values of voltage (V) and current (I).

$$\frac{\partial T}{\partial t} = \frac{2\pi\lambda S_W (T - T_0)^2}{\eta_a V I}. \qquad [7]$$

To calculate the cooling rate, the thermal conductivity of a Ni-Cr-Mo-W alloy with the addition of Fe was used, thus very similar to the Inconel 686 alloy. Besides this, the thermal conductivity was considered constant during solidification and the value used refers to a temperature of 973 K (700 °C), $\lambda \approx 17$ W/mK.[24] The arc electric efficiency used was $n_a = 0.67 \pm 0.05$.[25] Equilibrium diagrams were produced using the Thermo-Calc program, based on the composition of the melted zone of each clad. Thus, it was possible to estimate the beginning of the solidification temperature (T). Table V shows the estimated values for the beginning of the solidification temperature for each clad. Since all claddings had a similar beginning of the solidification temperature, the lowest value was used. Thereby, it is possible to reduce the problem to the

system, in which there is more time for diffusion to occur. The other parameters, S_w, T_0, V and I, were presented in Section II-B Experimental procedures.

The solidification range (T_s) used was approximately 394 K (121 °C), which refers to a Ni-Cr-Mo-W alloy, whose chemical composition is similar to that of the 686 alloy.[26] Table VI shows the estimated value for the cooling rate, using a beginning of the solidification temperature of 1643 K (1370 °C) and the respective t_s for the solidification range selected.

The value of a half of the secondary dendrite arm spacing was selected from the smallest average obtained. Thus, the calculation was optimized to have the biggest value of the parameter α. Therefore, 2.5 μm which is approximately a half value of the secondary dendrite arm spacing of S85 was used.

The diffusion coefficients of the elements were obtained from works[27–30] in which the elements were diffused into a Ni γ-CFC matrix. Table VII shows the diffusion coefficients of each element and its respective parameters α, using the t_s value shown in Table VI.

Parameter α showed extremely low values for all elements assessed, even under the most favorable conditions for diffusion. Therefore, the diffusion in the solid during the solidification of the weld metal was not relevant to calculate the microsegregation. Thus, the microsegregation calculation is reduced to the Scheil's equation.

To perform this calculation, the chemical composition of the dendrites and the composition of the melted zone were measured for each cladding. Tables VIII and IX show the average and the standard deviation measures of the EDS chemical composition of the center of the dendrites and the melted zone of the each cladding, respectively. It is important to highlight that the method

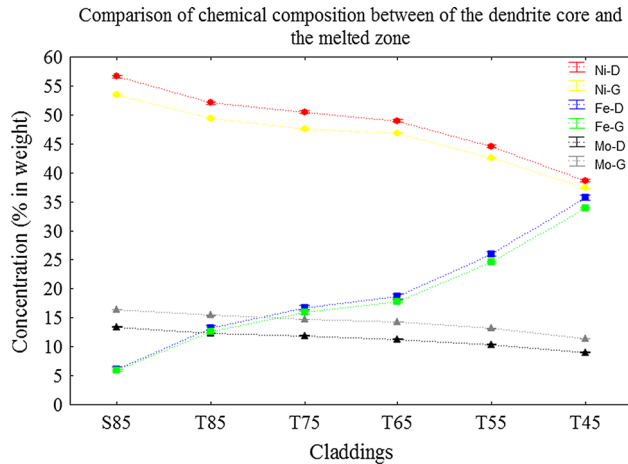|	Partition Coefficient (k)					
Elements	S85	T85	T75	T65	T55	T45
Cr	0.98 ± 0.00	0.99 ± 0.00	0.99 ± 0.01	0.98 ± 0.01	0.96 ± 0.02	0.96 ± 0.01
Fe	1.04 ± 0.09	1.05 ± 0.02	1.06 ± 0.06	1.07 ± 0.04	1.06 ± 0.07	1.05 ± 0.02
Ni	1.06 ± 0.01	1.05 ± 0.00	1.06 ± 0.01	1.05 ± 0.01	1.05 ± 0.02	1.04 ± 0.01
Mo	0.82 ± 0.01	0.80 ± 0.01	0.81 ± 0.01	0.79 ± 0.01	0.79 ± 0.02	0.79 ± 0.01
W	1.02 ± 0.01	1.01 ± 0.01	1.03 ± 0.02	1.01 ± 0.01	0.99 ± 0.02	0.98 ± 0.01

Fig. 9—Comparative graph between the chemical composition of the dendrites and melted zone. "D" and "FZ" show the concentration of the dendrite and molten zone, respectively.
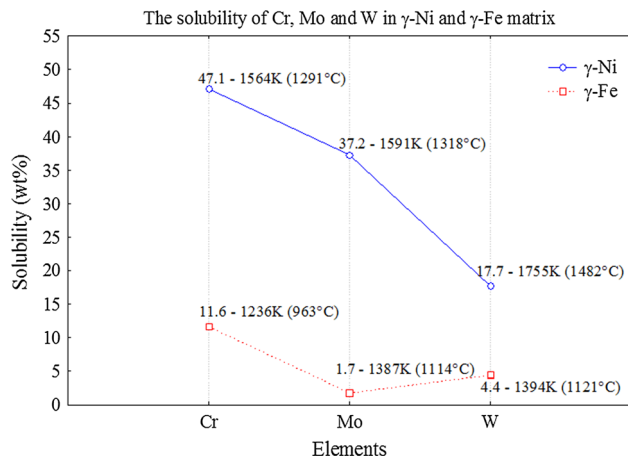

Fig. 10—Comparative graph showing the maximum solubility among the elements Cr, Mo, and W, in the γ-Ni and γ-Fe phases.

adopted to measure the dendrite composition selected a finite volume of material. However, the statistical results show a low dispersion, indicating that measurements can be close to the intended.

Comparing the chemical composition of the dendrites and the chemical composition of the melted zone, it is possible to observe that the microchemical changes were caused by microsegregation. Mo showed a lower concentration in the center of the dendrites than in the melted zone, thus, highlighting its tendency to segregate to the liquid. Figure 9 shows a graph comparing the chemical composition of the dendrites with the chemical composition of the molten zone for the elements with more significant changes (Fe, Ni e Mo).

Figure 9 clearly shows not only the microchemical changes of Mo, but also the tendency of Ni and Fe to be incorporated by the solid during solidification. The partition characteristics of these elements during solidification is similar to what has been previously reported in the literature in studies that evaluated the microstructure of the weld metal of Ni-Cr-Mo superalloys, similar to the Inconel 686, Hastelloy C-276 and Inconel 622 alloys.[14–16]

Table X shows the average and standard deviation of the partition coefficient (k) of the elements Cr, Fe, Ni, Mo, and W. The values of the coefficient (k) obtained for Ni and Fe were higher than 1, which shows the characteristic of these elements of being incorporated into the solid.[14–16] In general, Fe showed an increase in its k value as dilution increased. Banovic[16], when evaluating claddings with a deposit of the Inconel 622 and Inconel 625 alloys in various mixtures, observed this increase in the partition coefficient of Fe with an increase in dilution. Ni, in turn, showed a slight decrease in its k value with an increase in dilution. Mo showed a coefficient k lower than 1 in all claddings,[14–16,31,32] thus indicating its tendency to segregate to the liquid. In addition, Mo increased its segregation potential as dilution increased. The decrease of the coefficient k of Mo with the increase of dilution has been already observed in other studies.[16,32] Cr and W followed a behavior similar to that observed for Ni, showing a slight decrease of the coefficient k as dilution increased. In all claddings, both Cr and W had coefficients k close to 1.[31] Maltin,[33] from the deposition of the Inconel 686 alloy, observed that the coefficient k of W decreased with the increase of dilution. In a similar way, this reduction of the coefficient k of Cr with the increase of dilution has already been reported in previous studies.[16]

The effects of dilution on the segregation potential (k) are partially associated with the phenomenon of the solubility reduction of these elements in the new matrix γ-CFC, because now there is more iron in the matrix due to the dilution. The phase diagrams for the binary alloys Ni-Mo, Fe-Mo, Ni-Cr, Fe-Cr, Ni-W, and Fe-W show some differences in the solubility of the elements Mo, Cr, and W into the γ-Ni and γ-Fe matrices.[34] Figure 10 highlights the graphic form and the maximum solubility

of each element in the γ-Ni and γ-Fe matrices, according to the phase diagrams used.

The element Cr in the Ni-Cr system has a maximum solubility of approximately 47 pct in the γ-Ni matrix, at a temperature of 1564 K (1291 °C). In the Fe-Cr system, the solubility in the γ-Fe matrix is approximately 12 pct at a temperature of 1236 K (963 °C). Therefore, in binary systems, the matrix γ-Fe cannot solubilize high percentages of Cr. Thus, the addition of Fe reduces the solubility of Cr, favoring microsegregation and, consequently, the formation of deleterious phases, such as the σ phase, which has FeCr as its main stoichiometric formula.[35]

In the Ni-Mo system, the matrix γ-Ni is able to solubilize approximately 37 pct of Mo at a temperature of 1591 K (1318 °C), while in the γ-Fe system, approximately only 2 pct can be solubilized. This dramatic decrease favors the formation of topologically compact phases, which notably increase the susceptibility to corrosion in the interface between matrix and precipitate.[14,22] It is important to highlight that Mo is one of the main elements that increase resistance to corrosion with the important role of promoting a repassivation of the oxide film, which, in turn, protects the material surface.[4]

W, in turn, also has a higher solubility in the Ni-W system than in the Ni-Fe system, reaching a high solubility of approximately 18 pct in the γ-Ni matrix, and only 4 pct in the γ-Fe matrix. Again, this decrease in the ability to solubilize an alloying element can reduce the resistance to corrosion of the cladding, because, similarly to Mo, W increases resistance to crevice corrosion.[4] Furthermore, the addition of Fe not only favors the microsegregation of W, but also expands the μ phase stability field, since its main stoichiometry is Fe_6W_7.[36,37]

This evaluation methodology takes into account only binary systems in equilibrium. However, considering the high magnitude of the changes in solubility, the addition of Fe possibly caused a reduction in the solubility of the elements Mo, Cr, and W in the matrix of the cladding. Thus, the analyses of the phase diagrams corroborate with the values shown in Table X.

The results of the partition coefficient do not show any significant differences regarding the kind of weave (spiral and triangular). The comparison between the S85 and T85, which have the same wire feeding speed and heat input, with the only differences being in the kind and amplitude of weave, show the same partition coefficients for each element. The purpose of this work was to evaluate the changes in the cladding compositions by changing the dilution levels, but applying the same heat input throughout the work and two different weaves (spiral and triangular). However, the changes of the composition were not enough to show relevant differences in the microsegregation for these dilution levels and their respective metallurgical conditions. A similar result was observed in the literature where

relevant changes in the microsegregation were observed only in dilution levels above 20 pct.[16]

IV. CONCLUSION

Based on the experimental results obtained in this study about dissimilar weld cladding by the TIG process with cold wire feed from the AWS ERNiCrMo-14 (Inconel 686) alloy, with various dilution levels, in which microsegregation was evaluated, it was possible to conclude as follows:

The melted zone of all the claddings showed a columnar dendritic microstructure with secondary phases in the interdendritic region.

The spiral weave (S85) promoted the highest cooling rate and, consequently, the smallest secondary dendrite arm spacing due to the motion of the source, which is a characteristic of this type of weave.

Based on calculations performed using classical theories of solidification, the diffusion in the solid during solidification was not relevant for the elements Cr, Fe, Ni, Mo, W, and Mn.

The changes observed in the dilution level and hence in the concentration of Fe, resulting in changes in the behavior of microsegregation of the main elements of the alloy.

Fe and Ni showed a tendency to compose dendrites ($k > 1$). The partition coefficient k of Fe increased with higher levels of dilution. Ni, in turn, showed a slight drop in the value of k with the increase in dilution.

Mo showed a predisposition to segregate to the liquid ($k < 1$) and, with the increase in dilution, there was a drop in the coefficient k of Mo.

Cr and W showed k values of approximately 1. These elements also showed a slight decrease in their coefficients k as dilution increased.

According to the binary phase diagrams simulated in equilibrium, the addition of Fe possibly reduced the solubility of the main elements of the alloy (Cr, Mo e W) in the γ matrix, thus, favoring microsegregation.

The spiral weave (S85) in comparison with the triangular weave (T85) did not promote differences in the microsegregation. The small increase of iron probably did not promote any significant differences in the solubility of elements in the solid and consequently no alterations in the microsegregation.

NOMENCLATURE

S_{wf}	Wire feeding speed
WA	Weave amplitude
D	Dilution
A_{BM}	Area of the base metal
A_{FM}	Area of filler metal
C_{FZ}	Concentration of Fe in the fusion zone
C_{BM}	Concentration of Fe in the base metal
C_{FM}	Concentration of Fe in the filler metal
C_S	Composition of the solid
C_0	Composition of the liquid
γ	Austenite phase
σ	Sigma phase
μ	Mu phase
f_S	Fraction of the solid
k	Partition coefficient
α	Fourier diffusion number
$\frac{\partial T}{\partial t}$	Cooling rate
t_s	Time of solidification
D_s	Diffusion coefficient
L	Half of the dendritic spacing
λ	Thermal conductivity
Sw	Welding speed
T	Temperature of beginning of solidification
T_0	Pre-heating and/or interpass temperature
n_a	Electric arc efficiency
V	Voltage
I	Current
T_s	Solidification range

REFERENCES

1. J.H. Perepezko: *Science*, 2009, vol. 326, pp. 1068–69.
2. T.M. Pollock and S. Tin: *J. Propuls. Power*, 2006, vol. 22, pp. 361–74.
3. A.K. Mishra, S. Ramamurthy, M. Biesinger, and D.W. Shoesmith: *Electrochim. Acta*, 2013, vol. 100, pp. 118–24.
4. A.C. Lloyd, J.J. Noël, S. McIntyre, and D.W. Shoesmith: *Electrochim. Acta*, 2004, vol. 49, pp. 3015–27.
5. P. Jakupi, F. Wang, J.J. Noël, and D.W. Shoesmith: *Corros. Sci.*, 2011, vol. 53, pp. 1670–79.
6. C.C. Silva, C.R.M. Afonso, A.J. Ramirez, M.F. Motta, H.C. Miranda, and J.P. Farias: *Rev. Soldag. Insp.*, 2012, vol. 17, pp. 251–63.
7. R.M. Deacon, J.N. DuPont, and A.R. Marder: *Mater. Sci. Eng. A*, 2007, vols. 460–461A, pp. 392–402.
8. J.N. DuPont: *Metall. Mater. Trans. A*, 1996, vol. 27A, pp. 3612–20.
9. H. Naffakh, M. Shamanian, and F. Ashrafizadeh: *Metall. Mater. Trans. A*, 2008, vol. 39A, pp. 2403–15.
10. C.C. Silva, H.C. Miranda, M.F. Motta, J.P. Farias, C.R.M. Afonso, and A.J. Ramirez: *J. Mater. Res. Technol.*, 2013, vol. 2, pp. 228–37.
11. J.S. Ogborn, D.L. Olson, and M.J. Cieslak: *Mater. Sci. Eng. A*, 1995, vol. 203A, pp. 134–39.
12. M. Qian and J.N. DuPont: *Corros. Sci.*, 2010, vol. 52, pp. 3548–53.
13. F.G. Hodge: *JOM*, 2006, vol. 58, pp. 28–31.
14. C.C. Silva: *Revestimentos de ligas de níquel depositadas pelo processo TIG com alimentação de arame frio - aspectos operacionais e metalúrgicos*, pp. 39–265, PhD thesis, Universidade Federal do Ceará, Fortaleza, 2010.
15. W.M. Aguiar: *Revestimento por soldagem mig/mag empregando ligas de níquel para aplicações em componentes soldados do setor de petróleo e gás natural*, pp. 48–231, PhD thesis, Universidade Federal do Ceará, Fortaleza, 2010.
16. S.W. Banovic, J.N. Dupont, and A.R. Marder: *Sci. Technol. Weld. Join.*, 2002, vol. 7, pp. 374–83.
17. Y. Ahn, B. Yoon, H. Kim, and C. Lee: *Met. Mater. Int.*, 2002, vol. 8, pp. 469–77.
18. C.C. Silva, E.C. Miranda, M.F. Motta, H.C. Miranda, J.P. Farias: Dilution control of weld overlay superal overlay superal superalloys using taguchi method In *31st International Conference on Ocean, Offshore and Artic Engineering—OMAE*, ASME, Rio de Janeiro, 2012, pp 1–13.
19. C.C. Silva, E.C. Miranda, M.F. Motta, H.C. Miranda, and J.P. Farias: *Rev. Soldag. Insp.*, 2014, vol. 19, pp. 323–32.
20. E.C. Miranda, C.C. Silva, M.F. Motta, H.C. Miranda, and J.P. Farias: *Rev. Soldag. Insp.*, 2015, vol. 20, pp. 180–90.
21. H.D. Brody and M.C. Flemings: *Trans. Metall. Soc. AIME*, 1966, vol. 236, pp. 615–24.
22. C.C. Silva, C.R.M. Afonso, H.C. Miranda, A.J. Ramirez: *Technol. Metal. Mater. Min.*, 2011, vol. 8.
23. E. Scheil: *Z. Metallkd.*, 1942, vol. 34, pp. 70–72.
24. G. Yuquan, W. Dongjiang, M. Guangyi, and G. Dongming: *Rare Met. Mater. Eng.*, 2014, vol. 43, pp. 2663–68.
25. J.N. DuPont and A.R. Marder: *Weld. J.*, 1995, vol. 74, pp. 406s–16s.
26. M.J. Cieslak, T.J. Headley, and A.D. Romig: *Metall. Trans. A*, 1986, vol. 17, pp. 2035–47.
27. R.A. Swalin and A. Martin: *Trans. Metall. Soc. AIME*, 1956, vol. 8, pp. 567–72.
28. A. Davin, V. Leroy, D. Coutsouradis, and L. Habraken: *Mem. Sci. Rev. Metall.*, 1963, vol. 60, pp. 275–84.
29. B. Million, J. Růžičková, J. Velíšek, and J. Vřešťál: *Mater. Sci. Eng.*, 1981, vol. 50, pp. 43–52.
30. A.B. Vladimirov, V.N. Kaigorodov, S.M. Klotsman, and I.S. Trachtenberg: *Volume Diffusion of Simple and Transition Metal Impurities in Nickel monocrystals in Diffusion* and *Defect Monography Series*, Tihany, 1983, pp. 338–41.
31. M.J. Perricone and J.N. Dupont: *Metall. Mater. Trans. A*, 2006, vol. 37A, pp. 1267–80.
32. A.W. Stockdale and J.N. DuPont: *Sci. Technol. Weld. Join.*, 2011, vol. 16, pp. 426–32.
33. C. Maltin, A. Galloway, and M. Mweemba: *Metall. Mater. Trans. A*, 2014, vol. 45A, pp. 3519–32.
34. H. Okamoto, P. Nash, A.F. Guillermet, S.V.N. Naidu, A.M. Sriramamurthy, and P.R. Rao: *Alloy Phase Diagram*, ASM International, Youngstown, 1992, vol. 3, pp. 682–1244.
35. J.M. Joubert: *Prog. Mater. Sci.*, 2008, vol. 53, pp. 528–83.
36. J.M. Joubert and N. Dupin: *Intermetallics*, 2004, vol. 12, pp. 1373–80.
37. J.B. Forsyth and L.M. d'Alte da Veiga: *Acta Crystallogr.*, 1962, vol. 15, pp. 543–46.